

# Study of the response of $^{10}\text{B}$ -doped MCP to wide-energy range neutrons from eV to MeV\*

Qiang Li,<sup>1,2,3,†</sup> Li-Jiao Wang,<sup>1,2,4</sup> Xiang-Biao Qiu,<sup>5</sup> Jing-Wen Li,<sup>5</sup> Wei Xu,<sup>5</sup> Tao Li,<sup>5</sup> Ze-Bin Lin,<sup>6</sup> Chang-Jun Ning,<sup>1,2</sup> Yong-Hao Chen,<sup>1,2</sup> Rui-Rui Fan,<sup>1,2,3</sup> Kang Sun,<sup>1,2</sup> Jing-Yu Tang,<sup>7,8,‡</sup> Rong Zhang,<sup>5</sup> Han-Tao Jing,<sup>1,2</sup> Bo Mei,<sup>6</sup> Qi An,<sup>8,9</sup> Hao-Fan Bai,<sup>10</sup> Jiang-Bo Bai,<sup>11</sup> Jie Bao,<sup>12</sup> Ping Cao,<sup>7,8</sup> Qi-Ping Chen,<sup>11</sup> Zhen Chen,<sup>8,9</sup> Zeng-Qi Cui,<sup>10</sup> An-Chuan Fan,<sup>13</sup> Chang-Qing Feng,<sup>8,9</sup> Fan-Zhen Feng,<sup>13</sup> Ke-Qing Gao,<sup>1,2</sup> Min-Hao Gu,<sup>1,3</sup> Chang-Cai Han,<sup>14</sup> Zi-Jie Han,<sup>11</sup> Guo-Zhu He,<sup>12</sup> Yong-Cheng He,<sup>1,2</sup> Yang Hong,<sup>1,2,15</sup> Yi-Wei Hu,<sup>10</sup> Han-Xiong Huang,<sup>12</sup> Wei-Hua Jia,<sup>1,2</sup> Hao-Yu Jiang,<sup>10</sup> Wei Jiang,<sup>1,2</sup> Zhi-Jie Jiang,<sup>8,9</sup> Zheng-Yao Jin,<sup>13</sup> Ling Kang,<sup>1,2</sup> Bo Li,<sup>1,2</sup> Chao Li,<sup>8,9</sup> Gong Li,<sup>13</sup> Jia-Wen Li,<sup>8,9</sup> Xiao Li,<sup>1,2</sup> Yang Li,<sup>1,2</sup> Jie Liu,<sup>10</sup> Rong Liu,<sup>11</sup> Shu-Bin Liu,<sup>8,9</sup> Guang-Yuan Luan,<sup>12</sup> Bin-Bin Qi,<sup>8,9</sup> Jie Ren,<sup>12</sup> Zhi-Zhou Ren,<sup>11</sup> Xi-Chao Ruan,<sup>12</sup> Zhao-Hui Song,<sup>14</sup> Zhi-Xin Tan,<sup>1,2</sup> Sheng-Da Tang,<sup>1,2,6</sup> Peng-Cheng Wang,<sup>1,2</sup> Zhao-Hui Wang,<sup>12</sup> Zhong-Wei Wen,<sup>11</sup> Xiao-Guang Wu,<sup>12</sup> Xuan Wu,<sup>1,2</sup> Li-Kun Xie,<sup>8,9</sup> Yi-Wei Yang,<sup>11</sup> Han Yi,<sup>1,2</sup> Yong-Ji Yu,<sup>1,2</sup> Guo-Hui Zhang,<sup>10</sup> Lin-Hao Zhang,<sup>1,2</sup> Mo-Han Zhang,<sup>1,3</sup> Qi-Wei Zhang,<sup>12</sup> Xian-Peng Zhang,<sup>14</sup> Yu-Liang Zhang,<sup>1,2</sup> Yue Zhang,<sup>1,2</sup> Zhi-Yong Zhang,<sup>8,9</sup> Mao-Yuan Zhao,<sup>8,9</sup> Lu-Ping Zhou,<sup>1,2</sup> Zhi-Hao Zhou,<sup>1,2,15</sup> and Ke-Jun Zhu<sup>1,3,15</sup>

<sup>1</sup>*Institute of High Energy Physics, Chinese Academy of Sciences (CAS), Beijing 100049, China*

<sup>2</sup>*Spallation Neutron Source Science Center, Dongguan 523803, China*

<sup>3</sup>*State Key Laboratory of Particle Detection and Electronics,*

*Institute of High Energy Physics Chinese Academy of Sciences, Beijing 100049, China*

<sup>4</sup>*Dongguan Songshan Lake Future School, Dongguan 523808, China*

<sup>5</sup>*North Night Vision Science & Technology (Nanjing) Research Institute Co. Ltd., Nanjing 211106, China*

<sup>6</sup>*Sino-French Institute of Nucl. Eng. Technol., Sun Yat-sen University, Zhuhai 519082, China*

<sup>7</sup>*School of Nuclear Science and Technology, University of Science and Technology of China, Hefei 230027, China*

<sup>8</sup>*State Key Laboratory of Particle Detection and Electronics,*

*University of Science and Technology of China, Hefei 230026, China*

<sup>9</sup>*Department of Modern Physics, University of Science and Technology of China, Hefei 230026, China*

<sup>10</sup>*State Key Laboratory of Nuclear Physics and Technology,*

*School of Physics, Peking University, Beijing 100871, China*

<sup>11</sup>*Institute of Nuclear Physics and Chemistry, China Academy of Engineering Physics, Mianyang 621900, China*

<sup>12</sup>*Key Laboratory of Nuclear Data, China Institute of Atomic Energy, Beijing 102413, China*

<sup>13</sup>*USTC archaeometry lab, University of Science and Technology of China, Hefei 230026, China*

<sup>14</sup>*Northwest Institute of Nuclear Technology, Xi'an 710024, China*

<sup>15</sup>*University of Chinese Academy of Sciences, Beijing 100049, China*

Neutron-sensitive microchannel plates (nMCPs) have applications in neutron detection, including energy spectrum measurements, neutron-induced cross-sections, and neutron imaging.  $^{10}\text{B}$ -doped MCPs (B-MCPs) have attracted significant attention owing to their potential for exhibiting a high neutron detection efficiency over a large neutron energy range. Good spatial and temporal resolutions are useful for neutron energy-resolved imaging. However, their practical applications still face many technical challenges. In this study, a B-MCP with 10 mol%  $^{10}\text{B}$  was tested for its response to wide-energy neutrons from eV to MeV at the Back-n white neutron source at the China Spallation Neutron Source. The neutron detection efficiency was calibrated at 1 eV, which is approximately 300 times that of an ordinary MCP and indicates the success of  $^{10}\text{B}$  doping. The factors that caused the reduction in the detection efficiency were simulated and discussed. The neutron energy spectrum obtained using B-MCP was compared with that obtained by other measurement methods, and showed very good consistency for neutron energies below tens of keV. The response is more complicated at higher neutron energy, at which point the elastic and non-elastic reactions of all nuclides of B-MCP gradually become dominant. This is beneficial for the detection of neutrons, as it compensates for the detection efficiency of B-MCP for high-energy neutrons.

Keywords: Neutron radiation image;  $^{10}\text{B}$  doped MCP; Neutron response; wide-energy range neutrons

## I. INTRODUCTION

Neutron energy-resolved imaging (NERI), such as Bragg-edge imaging with thermally cold neutrons and resonance

imaging with epithermal fast neutrons, is a powerful method for studying the microstructures of materials and has become an attractive method in the field of neutron imaging in recent years. For decades, detector technologies for neutron imaging, such as scintillator arrays, position-sensitive gas detectors, as well as CCD and CMOS cameras, have been limited by the neutron detection efficiency and could not fully meet the requirements of NERI [1–7]. Neutron-sensitive microchannel plates (nMCPs) have good spatial and temporal resolution as well as the potential for high neutron detection efficiency. Recent developments in nMCPs have expanded

\* This work was supported by the Guangdong Basic and Applied Basic Research Foundation (No. 2023A1515030074) and the National Natural Science Foundation of China (Project 12035017).

† Corresponding author, qiangli@ihep.ac.cn(Qiang Li)

‡ Corresponding author, jytang@ustc.edu.cn(Jing-Yu Tang)

the capability of the NERI method and are probably the most cutting-edge method in the field of neutron photography [8–11].

In 1990, Fraser and Pearson first proposed the nMCP and doped  ${}^6\text{Li}_2\text{O}$  into MCP to obtain a thermal neutron detection efficiency of only 0.21% [12]. Since then,  ${}^{10}\text{B}$  and  ${}^{nat}\text{Gd}$  with larger thermal neutron cross sections have been used as the main doping materials [13, 14]. For example, Tsinghua University developed an event-counting thermal neutron imaging detector using an nMCP doped with 3 mol%  ${}^{nat}\text{Gd}_2\text{O}_3$ ; the thermal neutron detection efficiency reached 33% [15]. Harbin Engineering University used mixed doping of 10 mol%  ${}^{10}\text{B}_2\text{O}_3$  and 0.4 mol%  ${}^{nat}\text{Gd}_2\text{O}_3$  to achieve a thermal neutron detection efficiency of 28%, which was better than that doped with  ${}^{10}\text{B}$  only [16]. The products  $\alpha$  and  ${}^7\text{Li}$  of the  $(\text{n}, {}^{10}\text{B})$  reaction have stopping ranges of approximately 2–3.5  $\mu\text{m}$  in the MCP [17], whereas the product  $\gamma$  of the  $(\text{n}, {}^{nat}\text{Gd})$  reaction has a range of approximately 100  $\mu\text{m}$ . Therefore,  ${}^{10}\text{B}$ -doped nMCPs have a relatively higher spatial resolution than those doped with  ${}^{nat}\text{Gd}$ . On the other hand,  ${}^{10}\text{B}$  has higher and smoother reaction cross-sections for a neutron energy above the epithermal region, which is more suitable than  ${}^{nat}\text{Gd}$ , especially for epithermal-fast neutron resonance imaging. Increasing the doping concentration to B detection efficiency of up to 60% for thermal neutrons.  ${}^{10}\text{B}$  However, until now, the development of MCPs with high concentrations of  ${}^{10}\text{B}$  has been difficult because excessive  ${}^{10}\text{B}$  corrodes the MCP glass substrate during the process [19].  ${}^{10}\text{B}$ -doped nMCPs (B-MCP), developed by U. C. Berkeley, NOVA Corporation, Tsinghua University, etc., are mainly used in thermal-cold neutron imaging [20–22]. However, neutron resonance imaging in a wide energy region from eV to MeV has higher detection efficiency requirements and must solve the complex response problem of B-MCP to high-energy neutrons.

This paper presents a study on the detection efficiency and responses of a B-MCP to wide-energy neutrons from eV to MeV at the Back-n white neutron source of the China Spallation Neutron Source (CSNS). Back-n provides a white neutron beam with a wide energy spectrum, high neutron flux, and good temporal resolution for serving as a multipurpose platform to support nuclear data measurements, detector calibrations, and neutron photography [23–26]. The main factors affecting the detection efficiency loss of the B-MCP, signal sources in the B-MCP output, and the contribution of different reactions to the neutron detection efficiency in different energy regions were analyzed. The results provide a basis for the ongoing development of B-MCP for neutron imaging, especially for energy-resolved imaging over a wide energy range.

## II. EXPERIMENTAL SETUP

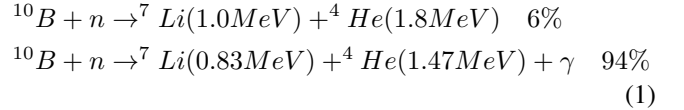
The B-MCP used in the experiment was developed in cooperation with North Night Vision, and its main parameters are listed in Table 1.

The B-MCP contains approximately 10 mol%  ${}^{10}\text{B}$  from the glass substrate doping, and composition measurements

Table 1. The main parameters of the B-MCP and an ordinary MCP.

Parameters	B-MCP	Ordinary MCP
Diameter(mm)	33	33
Thickness(mm)	0.515	0.62
Body resistance( $\text{M}\Omega$ )	81	146
Pore inner diameter( $\mu\text{m}$ )	8	10
Pore area ratio (%)	60	60
Gain	$1915@800\text{V}$	$1.3 \times 10^5@1200\text{V}$
${}^{10}\text{B}$ (mol%)	10	—

show that the preparation process does not induce a significant boron loss. The ordinary MCP also contains trace amounts of approximately 0.15% natural boron (19.78%  ${}^{10}\text{B}$  and 80.22%  ${}^{11}\text{B}$ ) originating from the preparation process (not shown in the table). The gain of the B-MCP is approximately two orders of magnitude lower than that of an ordinary MCP, which is beneficial for neutron detection. A large gain in a B-MCP would lead to an excessive amplitude range of neutron signals, which is not conducive to the efficient acquisition of neutron events with specifically designed electronics that have a limited dynamic range. Therefore, the B-MCP should reduce the gain appropriately and work in unison with an ordinary MCP to obtain the required total signal gain. To improve the secondary electron efficiency and reduce the ion feedback, MCP pores have a bevel angle of approximately  $5^\circ \sim 12^\circ$  and are stacked in the V-shape of the two MCPs. The nuclear reactions of  ${}^{10}\text{B}$  with incident neutrons are expressed by Eq. (1).



The simulations (Sec. IV) indicate that a large amount of  $\alpha$  or  ${}^7\text{Li}$ , which can penetrate the substrate, enter one or more pores of the B-MCP and excite the primary electrons on the inner wall. When a specified electric field is applied to the MCPs, the electrons multiply many times in the pores to form an electron cloud at the exit surface of the MCP. The electron cloud is generally sufficiently strong such that it can be collected by the collector electrode. The obtained primary signal reflects the response of the B-MCP to neutrons. In this experiment, a single-anode PCB board was used as the B-MCP signal collector electrode; the package structure of the B-MCP detector is shown in Fig. 1.

The main structure includes a ceramic cover, cushion, four voltage-partition electrodes, a V-shaped B-MCP/MCP stack, a ceramic base, and an anode PCB board. The ceramic cover and base serve as external structures that provide integrated packaging. Four copper ring electrodes are used to apply voltage to both sides of the B-MCP and MCP, and the cushioned copper ring protects the B-MCP/MCP stack from being oversqueezed. An ordinary MCP/MCP stack with the same package structure is used for comparison. The resistor series are used to divide the voltage, and the voltage ratio of the B-MCP and the MCP is 0.9:1 for the B-MCP detector and 1:1 for the MCP detector. The anode is grounded using a  $2\text{-M}\Omega$  resistor.

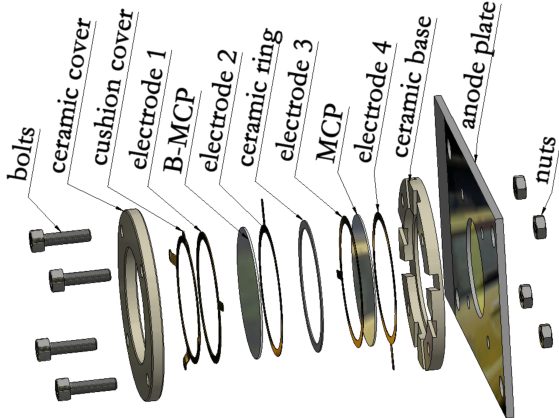


Fig. 1. Schematic diagram of the B-MCP mechanical package structure.

The experimental layout of the B-MCP at the Back-n white-neutron source is shown in Fig. 2. The B-MCP (or MCP) detector is mounted on a bracket that allowed the neutron beam to pass perpendicularly through the center of the MCP. The surface of the B-MCP is located approximately 58 m from the spallation target. The beam profile at the detector is set to  $\Phi 20$  mm, which is smaller than the diameter of the B-MCP, thus allowing the neutron beam to pass completely through the sensitive area of the detector. The neutron flux is approximately  $1.87 \times 10^6$  neutrons/cm $^2$ /s, and the energy range covers 0.5 eV-200 MeV [27, 28]. The B-MCP detector and preamplifier (Mesytec MPR-1) were placed inside the vacuum chamber of the LPDA spectrometer [29]. The experiment used the common electronics and data acquisition systems of the Back-n facility [30, 31]. The output signals of the preamplifier were digitized by the readout electronics system with a 12 bit folding-ADC and a 1 GHz sampling rate [32]. The system was triggered by the T0 signal from the proton beam monitor, and the threshold was set to 14.6 mV to filter the electronic noise. The sampling duration was set from 2  $\mu$ s before the T0 trigger to 8  $\mu$ s after the T0 trigger, and the waveform of each neutron event was recorded. Because it is difficult for MCPs to distinguish between dark counts and neutron events, the B-MCP uses a voltage of -1750 V to keep the dark counts below 0.1 cps/cm $^2$ . Each measurement took 10800 s to obtain accurate statistics.

### III. EXPERIMENTAL RESULTS AND ANALYSIS

Fig. 3 shows a typical signal waveform recorded immediately after the T0 trigger. The data analysis was performed using the ROOT program developed by CERN [33]. Owing to the long decay time of the preamplifier output, a signal pileup may occur within a sampling window of 10  $\mu$  second. To filter out noise and discriminate between effective events, we applied smoothing and differential transformation methods to the primary waveforms. The waveform after the differential transformation is presented, where the baseline of the differential waveform recovers to zero immediately after each

event pulse. This signal caused a sudden falling edge of the primary waveform, corresponding to a negative extremum after differentiation. By setting an appropriate threshold, these extrema can be selected to obtain signals within the sampling window. There were significantly more signals close to the T0 trigger than far from T0 because fast neutrons arrived in shorter flight times.

Fig. 4 shows the time-of-flight (TOF) pulse height (PH) correlation spectrum of the total B-MCP signals. Two event bands around 195  $\mu$ s and 605  $\mu$ s correspond to the double-bunch time structure of proton pulses from the CSNS accelerator and represent the  $\gamma$ -flash generated in the spallation target. The  $\gamma$ -flash detected by the B-MCP is also used to calibrate the T0 signal because the flight time of the  $\gamma$ -flash from the target to the B-MCP is 195  $\mu$ s. Small signal clusters before the  $\gamma$ -flash were considered random noise, whereas the signals between the  $\gamma$ -flash bands corresponded to high-energy neutrons from the first neutron bunch. Based on the noise, we set the signal threshold to a five ADC-code to obtain pure neutron events for the trend and structural analysis of the neutron energy-count spectrum. The data acquisition threshold of 14.6 mV resulted in the loss of some small neutron signals, causing a rare-event gap with a PH below 20 and TOF above approximately 24000 (corresponding to a neutron energy of approximately 30 keV). These events were sparse in time distribution and were less likely to be passively recorded with an adjacent large-signal trigger than neutrons in the higher-energy region.

The kinetic energy of neutrons can be calculated using Eq. (2):

$$E_n = (\gamma - 1)m_n c^2$$

$$\gamma = \frac{1}{\sqrt{1 - (\frac{v}{c})^2}} \quad (2)$$

where  $v = L_{\text{flight}}/\text{TOF}$ . The neutron flight length  $L_{\text{flight}}$  was corrected to 58.04 m using the resonance peaks in epithermal neutron region. The neutron energy-count spectra of the B-MCP and MCP detectors are shown in Fig. 5.

A large difference between the two curves is observed, particularly in the range of approximately 0.5 eV-30 keV, where the counts of the B-MCP are two orders of magnitude larger than those of the MCP, indicating the successful doping of  $^{10}\text{B}$  into the B-MCP. The trends of the two curves were almost constant in this region and gradually approached above 30 keV. Notably, the counting rate of the MCP increased significantly and was close to that of the B-MCP for neutron energies larger than MeV (reaching approximately 80% of the B-MCP). Simulations confirmed that above 30 keV, the contribution to the counts from the nuclear reactions by the other elements in both the B-MCP and ordinary MCP gradually increases. This result will be presented in Sec. IV. The intrinsic microstructure of the B-MCP curve below 30 keV reproduced the original energy spectrum of the Back-n neutron beam, which was confirmed by the retrieved energy-count spectrum of the B-MCP using the  $^{10}\text{B}$  ( $n, \alpha$ ) cross-section from the database [34] as shown in Fig. 6a. The two

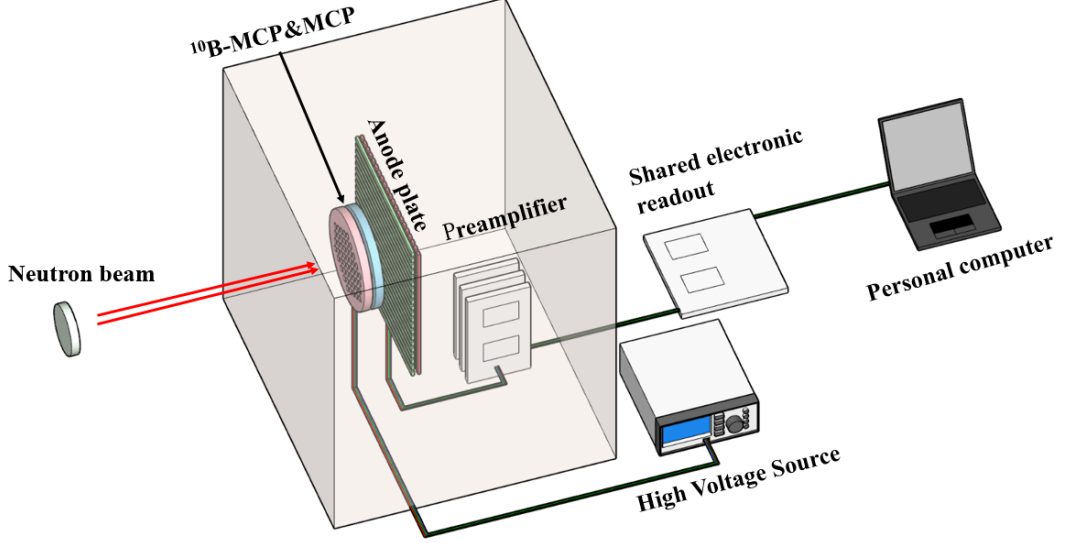


Fig. 2. Experimental layout of the B-MCP at the Back-n white neutron source.

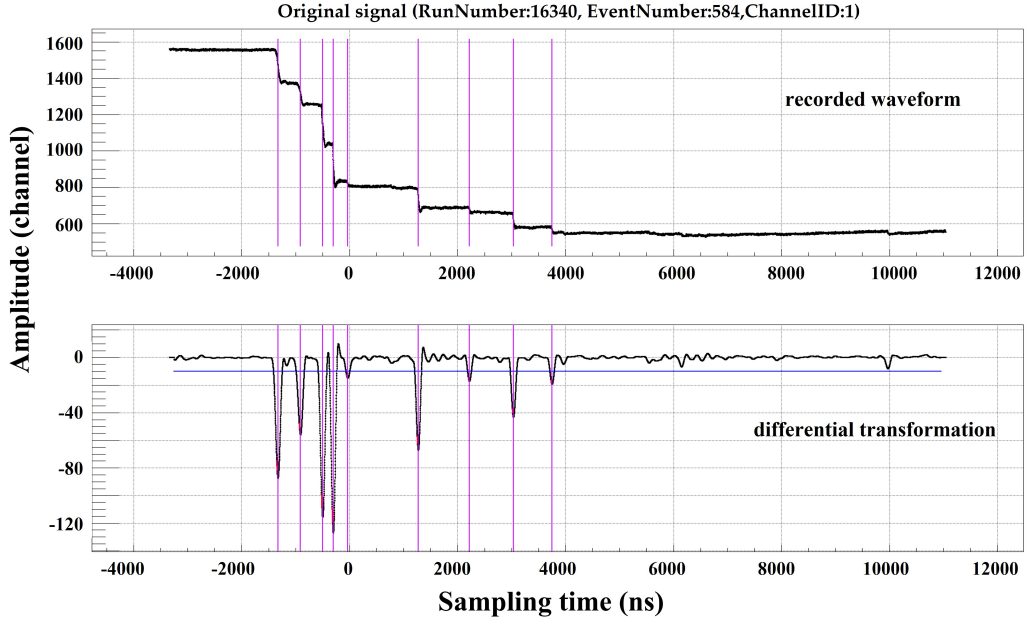


Fig. 3. A typical waveform recorded close the T0 trigger and its differential transformation.

normalized curves were consistent in both profile and structures below approximately 30 keV. The resonance peaks of some nuclides such as Ta, Mo, Mn, and Fe in the spallation target are marked. This confirms that events below 30 keV primarily originate from the doped  $^{10}\text{B}$ . Similar structures are also observed in the MCP spectrum, which are attributed to the small amount of natural boron contained in an ordinary MCP substrate. A similar energy count spectrum of the MCP using the  $^{10}\text{B}$  ( $n, \alpha$ ) section is shown in Fig. 6b. The two normalized curves were entirely consistent in the profile and roughly consistent in the structures below approximately 30 keV. However, the significant increase in counts above 30

keV was inconsistent with  $^{10}\text{B}$  ( $n, \alpha$ ) reactions. Additional complex responses were produced by the interaction of MCP components with higher-energy neutrons. The two curves in Fig. 5 have similar trends and structures above MeV, reflecting neither the Back-n spectrum nor the ( $n, \alpha$ ) cross-sections of  $^{10}\text{B}$ . These curves reflect the cross-sectional structures of the responding nuclides in the MCPs.

The detection efficiency of the B-MCP was calculated using Eq. (3) from eV to MeV, and the results are shown in Fig. 7.

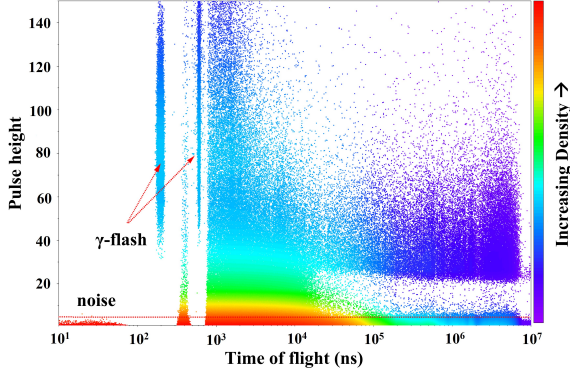


Fig. 4. The TOF-PH spectrum of the total B-MCP signals.

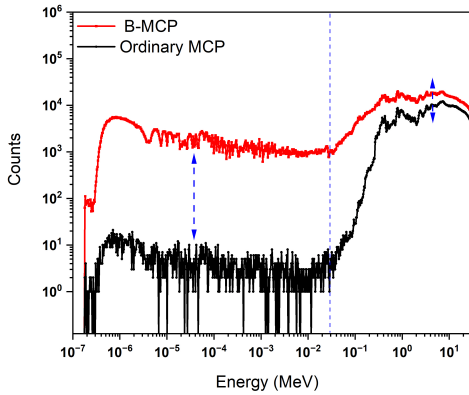


Fig. 5. The neutron energy-counts spectra measured by the B-MCP and the ordinary MCP.

$$\varepsilon = \frac{\eta_1 N_{exp}}{\eta_2 \Phi S_{\Phi} t} \quad (3)$$

where  $\Phi S_{\Phi} t$  is the total neutron flux in the B-MCP,  $\eta_1$  is the ratio of the measured counts in the energy bin to the total measured counts, and  $\eta_2$  is the ratio of neutron flux in the energy bin to the total neutron flux. We compare the detection efficiency with  $(n, \alpha)$  cross section of  $^{10}\text{B}$  [34] as a function of the neutron energy in same span of orders of magnitude. The two curves below 30 keV have the same decreasing trend, indicating that this part of the detection efficiency is from the  $(n, \alpha)$  reaction of  $^{10}\text{B}$ . The detection efficiency above 30 keV does not decrease with the cross-section of the  $^{10}\text{B}$ , which is due to additional complex responses from the MCP components, as analyzed in the Fig. 6.

Taking the detection efficiency of 1 eV neutron as a criteria, the counts with a PH threshold larger than five ADC-code corresponding to a neutron detection efficiency of about 0.38%. Although this is about 293 times larger than the ordinary MCP, it is far below expectation of 8% calculated using the  $^{10}\text{B}$  doping concentration. Primary waveform analysis suggests that a large number of neutron events with PH less

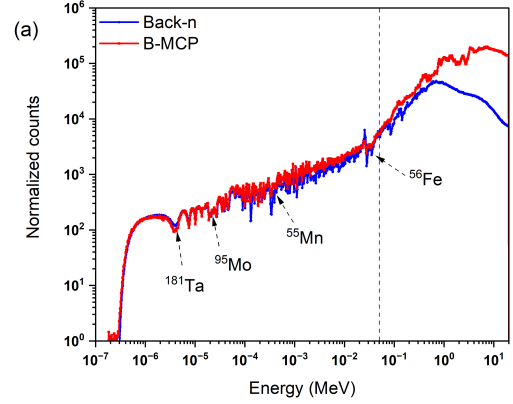


Fig. 6. The neutron energy spectrum measured by (a) the B-MCP and (b) the ordinary MCP, and their normalized comparison with the back-n spectrum.

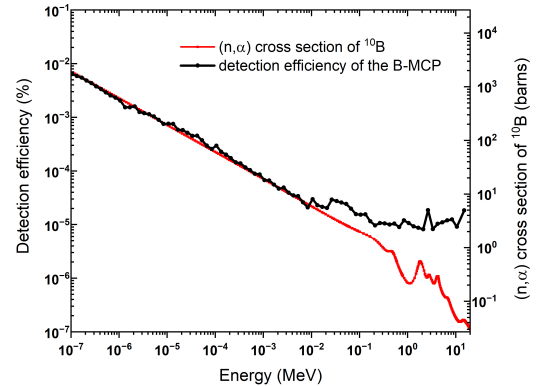


Fig. 7. Neutron detection efficiency of the B-MCP from eV to MeV and its comparison with  $(n, \alpha)$  cross section of  $^{10}\text{B}$ .

than five are not well separated from the noise. The efficiency loss may be due to several reasons. A major contribution is that some  $^{10}\text{B}$  reaction products cannot enter the MCP pores,

as the simulations suggest. There are also smaller neutron signals that are excluded by the data acquisition threshold of 14.6 mV. It is the inherent issue due to the gain of the B-MCP. The signal amplitude depends on the position where the primary electrons are generated in the B-MCP. The large gain of the B-MCP leads to thousand-fold difference in the amplitude of the signals, resulting in the inevitable presence of small signals that are excluded by the threshold due to mixing with noise. Reducing the B-MCP gain effectively compresses the amplitude range of neutron signals. Alternatively, increasing the ordinary MCP gain to saturate the signals can eliminate the amplitude differences. However, it is crucial to consider the distinction from noise, dark counts, etc.

#### IV. SIMULATION AND COMPARISON WITH THE EXPERIMENT

To further explore the detection efficiency and neutron response mechanism of B-MCP, the Monte Carlo code GEANT4 was employed to simulate the reactions of the B-MCP to the Back-n neutron beam. The FTFP\_BERT\_HP was used as the physics list of the process [35]. The components of the B-MCP are listed in Table 2.

Table 2. The mass percentage of the B-MCP components.

Components	Mass(%)
SiO <sub>2</sub>	43
<sup>10</sup> B <sub>2</sub> O <sub>3</sub>	8
PbO	24
Bi <sub>2</sub> O <sub>3</sub>	13
Al <sub>2</sub> O <sub>3</sub>	1.5
K <sub>2</sub> O	8
Na <sub>2</sub> O	1.5
BaO	1

SiO<sub>2</sub> is the primary substrate of the B-MCP, comprising approximately 43% of its mass. Bi<sub>2</sub>O<sub>3</sub> and PbO are used to adjust the resistance of the MCP to form an electron excitation layer, while Al<sub>2</sub>O<sub>3</sub> is to eliminate possible bubbles in the MCP and improves electron excitation. Other metallic oxide components can increase the hardness and strength of the MCP glass. The geometry of the B-MCP is illustrated in Fig. 8.

The arrangement of the B-MCP's pores is hexagonal structure similar to honeycomb [36], with an average distance between the pores of about 2-3  $\mu$ m, based on the pore diameter and area ratio. The actual B-MCP contains millions of pores, making it unrealistic to model the entire structure exactly. A local model with a diameter of approximately 100  $\mu$ m and hundreds of pores is sufficient to meet the simulation requirements. The Back-n energy spectrum [37] is used, and the beam diameter is set to 45  $\mu$ m to ensure that all neutrons pass perpendicularly through the B-MCP surface. The pores have a bevel angle of 8° to conform to the B-MCP object.

The total responses of the B-MCP are simulated with natural abundance of all the elements other than <sup>10</sup>B. These responses are divided by the (n, tot) cross-sections of the cor-

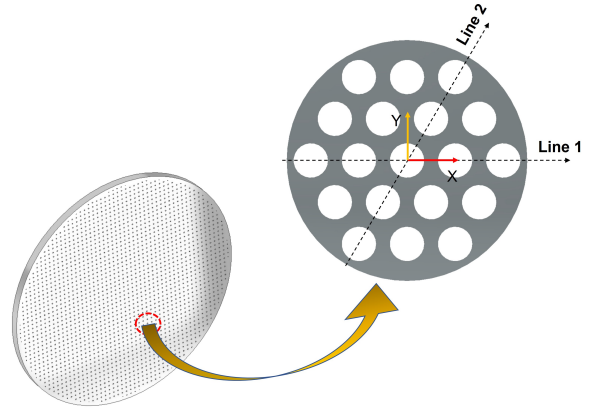


Fig. 8. Schematic diagram of the B-MCP geometry.

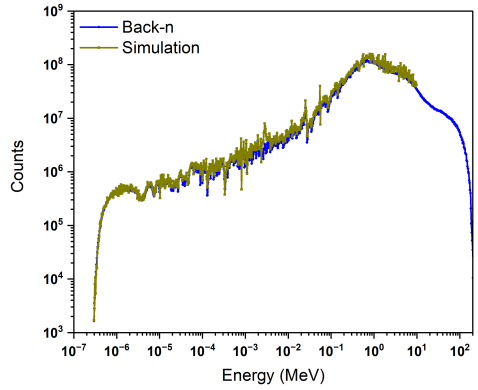


Fig. 9. The neutron energy spectrum simulated by using total responses of the B-MCP, and its normalized comparison with the back-n spectrum.

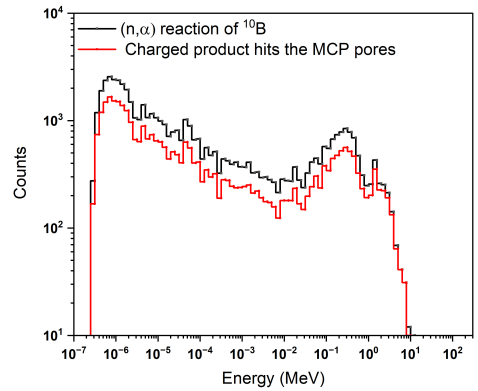


Fig. 10. The neutron energy-counts spectra simulated with total <sup>10</sup>B (n,  $\alpha$ ) reactions and with the signal cases in which charged products <sup>7</sup>Li or  $\alpha$  entering the MCP pores.

responding nuclides extracted from ENDF-B/VIII.0 to obtain

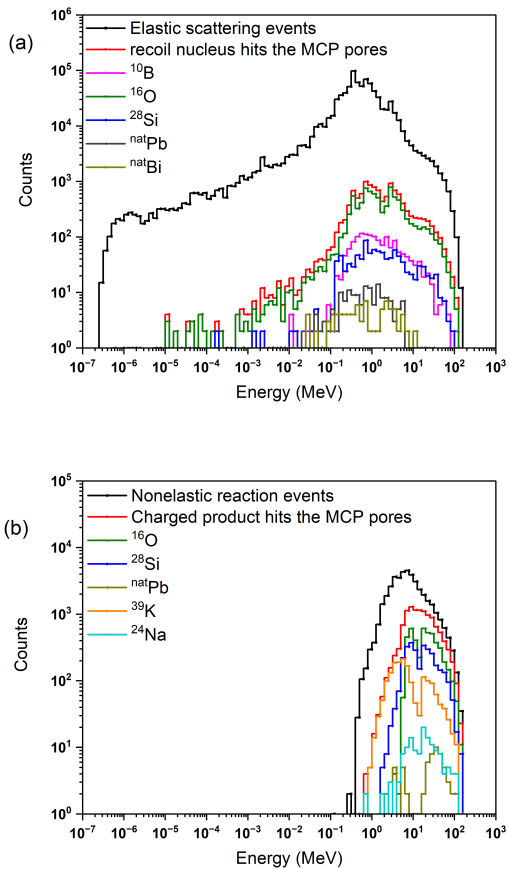


Fig. 11. The neutron energy-counts spectra simulated with: (a) total elastic scattering responses and their signal cases; (b) total nonelastic reactions and their signal cases.

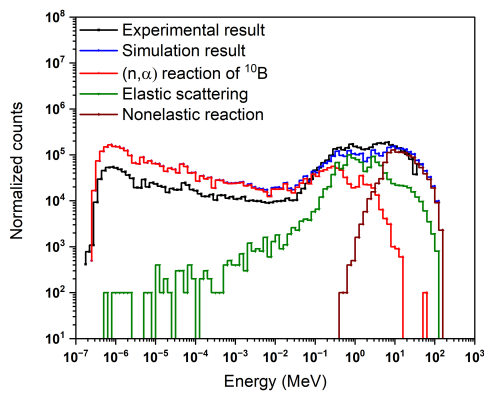


Fig. 12. The simulated total signal responses of the B-MCP and their normalized comparison with the experiment.

the neutron energy spectrum detected by B-MCP, which is compared with the original Back-n spectrum, as shown in Fig. 9 [34]. The two spectra exhibit consistent profile and

fine-structures, indicating that the simulation results are reliable. However, not all the responses can generate signals in the experiment. It is considered that only the charged products that enter the pores have good opportunity to excite primary electrons and produce signals. An experimental event requires that at least one or more of the charged products from the reaction pass through the inner wall into the pores.

The main reactions between neutrons and the B-MCP are categorized into three types: the  $(n, \alpha)$  reaction with  $^{10}\text{B}$ , elastic scattering with all the nuclides, and nonelastic reactions with all the nuclides other than  $^{10}\text{B}$ . The neutron energy-counts spectra for the total  $^{10}\text{B}$   $(n, \alpha)$  reactions and for the signal cases in which charged products  $^7\text{Li}$  or  $\alpha$  entering the pores are shown in Fig. 10. The proportion of signal cases is approximately 61% of the total  $^{10}\text{B}$   $(n, \alpha)$  reactions, which is considered one of the factors contributing to the loss of neutron detection efficiency in the experiment. It is observed that the proportion of signal cases in the energy range of about 0.5 eV - 300 keV remains relatively constant, which can be attributed to the fact that product energy is almost independent of neutron energy in the low-energy region. However, the proportion significantly increases at higher energy, because the product particles carry also the kinetic energy of the neutrons and increases the chance of entering the pores.

The neutron energy-counts spectra for total elastic scattering responses and for their signal cases in which recoil nuclei entering the pores are shown in Fig. 11a. Elastic scattering occurs in all neutron energy regions from eV to hundreds of MeV, but only cases with neutron energy above tens of keV have a chance of recoil nuclei entering the pores to generate signals. Recoil nuclei with low-energy neutrons do not gain sufficient kinetic energy. The lighter the nucleus, the easier it is to obtain higher recoil kinetic energy. The recoil nuclei entering the pores are mainly  $^{16}\text{O}$ , followed by  $^{28}\text{Si}$  and  $^{10}\text{B}$ . Moreover,  $^{16}\text{O}$  and  $^{28}\text{Si}$  are the main components of B-MCP. The total nonelastic reaction responses of the B-MCP and their signal cases in which secondary charged particles enter the pores are shown in Fig. 11b. Nonelastic reactions generally have a high reaction threshold and mainly occur with the neutron energy above several hundred keV.

The summation of all the signal cases described above is normalized to the experimental result, as shown in Fig. 12. Signal responses below 30 keV are mainly from  $^{10}\text{B}$   $(n, \alpha)$  reactions. Additional responses by the B-MCP components above 30 keV observed in the experiment are mainly attributed to the elastic scattering of  $^{16}\text{O}$ , accounting for about 75% of all the elastic scattering signals. Nonelastic reactions occur when neutron energies are greater than 0.5 MeV and contributes to the majority of the counts above 10 MeV. They are mainly  $^{16}\text{O}$   $(n, \alpha)$ ,  $^{28}\text{Si}$   $(n, p)$ ,  $^{39}\text{K}$   $(n, p)$ , etc., as shown in Fig. 11b. The nonelastic response signals of the above three nuclides as the main factor account for about 82% of the total nonelastic response signals. The simulation results are in general consistent to the experimental one for neutron energy above tens of keV. However, the experimental counts are significantly lower than the simulations in the lower energy region. This is consistent with the fact that loss of detection efficiency mainly occurs in the low energy region in the ex-

periment.

## V. CONCLUSIONS AND DISCUSSIONS

A B-MCP detector has been developed. It can be employed for different purposes, e.g., neutron-induced cross-section measurements, neutron energy spectrum measurement and neutron energy-resolved imaging. This study investigated the responses and detection efficiency of the B-MCP to wide-energy neutrons from eV to MeV at the Back-n using experiments and simulations. The measured detection efficiency is far less than the theoretical efficiency estimated with the  $^{10}\text{B}$  content. The reduction in efficiency is mainly due to that partial reaction products do not enter the MCP pores and some small signals do not reach the trigger threshold for record-

ing. The two reasons are inherent issues, with the former due to the doping method of  $^{10}\text{B}$  and the latter to the gain of the B-MCP. The former is confirmed by simulations. The simulations also confirm the response curve of the measured results, in particular the higher counts at neutron energy larger than 30 keV. The elastic and nonelastic reactions of all the nuclides of the B-MCP are found to contribute to the counts besides the  $^{10}\text{B}$  ( $n, \alpha$ ) reaction. This is in fact beneficial to compensate the natural reduction in detection efficiency by the  $^{10}\text{B}$  ( $n, \alpha$ ) reaction due to exponential decaying of the cross-section with respect to neutron energy.

The further efforts will be as follows: trying to obtain even higher  $^{10}\text{B}$  doping, optimization of the bias voltages, and developing a new electronics and data acquisition system to retrieve the X/Y/T information for neutron imaging.

---

[1] I Mor, D Vartsky, M Brandis et al., Fast-neutron imaging spectrometer based on liquid scintillator loaded capillaries. *JINST* **7**, C04021 (2012). [doi:10.1088/1748-0221/7/04/C04021](https://doi.org/10.1088/1748-0221/7/04/C04021)

[2] Ronald O. Nelson, Sven C. Vogel et al., Neutron Imaging at LANSCE—From Cold to Ultrafast. *J. Imaging* **4**, 45 (2018). <https://doi.org/10.3390/jimaging4020045>

[3] L.X. Zhang, S.Z. Chen, Z.D. Zhang et al., Resolution analysis of thermal neutron radiography based on accelerator-driven compact neutron source. *Nucl. Sci. Tech.* **34**, 76 (2023). <https://doi.org/10.1007/s41365-023-01227-x>

[4] C.B. Lu, J Bao, Y Huang et al., Contrast sensitivity in 14MeV fast neutron radiography. *Nucl. Sci. Tech.* **28**, 78 (2017). [doi:10.1007/S41365-017-0228-5](https://doi.org/10.1007/S41365-017-0228-5)

[5] K.Q. Gao, H. Yi, Q.M. Zhang et al., First experiment on neutron resonance radiography with a Micromegas detector at the Back-n white neutron source. *JINST* **16**, P02036 (2021). <https://doi.org/10.1088/1748-0221/16/02/P02036>

[6] X.S. Yan, Y.G. Yang, Q. Li et al., Combined gamma-ray and energy-selective neutron radiography at CSNS. *Nucl. Instr. Meth. A* **955**, 163200 (2020). <https://doi.org/10.1016/j.nima.2019.163200>

[7] L.J. Wang, Q. Li, J.Y. Tang et al., Experimental studies on nuclide identification radiography with a CMOS camera at Back-n white neutron source. *Nucl. Instr. Meth. A* **1048**, 167892 (2023). <https://doi.org/10.1016/j.nima.2022.167892>

[8] A.S. Tremsin, A.E. Craft, M.A.M. Bourke et al., Digital neutron and gamma-ray radiography in high radiation environments with an MCP/Timepix detector. *Nucl. Instr. Meth. A* **902**, 110–116 (2018). <https://doi.org/10.1016/j.nima.2018.05.069>

[9] A.S. Tremsin, J Rakovan, T Shinohara et al., Non-Destructive Study of Bulk Crystallinity and Elemental Composition of Natural Gold Single Crystal Samples by Energy Resolved Neutron Imaging. *Scientific Reports* **7**, 40759 (2017). <https://doi.org/10.1038/srep40759>

[10] J.Q. Yang, J.R. Zhou, L.J. Zhang et al., Recent measurements at the CSNS towards the construction of a nMCP detector for the energy resolved neutron imaging instrument. *Nucl. Instr. Meth. A* **1003**, 165322 (2021). <https://doi.org/10.1016/j.nima.2021.165322>

[11] A.S. Tremsin, A.E. Craft, G.C. Papaioannou et al., On the possibility to investigate irradiated fuel pins non-destructively by digital neutron radiography with a neutron-sensitive microchannel plate detector with Timepix readout. *Nucl. Instr. Meth. A* **927**, 109–118 (2019). <https://doi.org/10.1016/j.nima.2019.02.012>

[12] G. Fraser, J. Pearson, The direct detection of thermal neutrons by imaging microchannel-plate detectors. *Nucl. Instr. Meth. A* **293**, 569–74 (1990). [https://doi.org/10.1016/0168-9002\(90\)90325-Z](https://doi.org/10.1016/0168-9002(90)90325-Z)

[13] J.Q. Yang, J.R. Zhou, L.J. Zhang et al., Efficiency calculation of the nMCP with 10B doping based on mathematical models. *Nucl. Eng. Technol.* **53**, 2364–2370 (2021). <https://doi.org/10.1016/j.net.2021.01.026>

[14] Y. Tian, Y.G. Yang, J.S. Pan et al., High efficiency event-counting thermal neutron imaging using a Gd-doped micro-channel plate. *Chin. Phys. C* **38**, 086003(2014). [doi:10.1088/1674-1137/38/8/086003](https://doi.org/10.1088/1674-1137/38/8/086003)

[15] Y.M. Wang, Y Tian, Y.G. Yang et al., Detection efficiency evaluation for a large area neutron sensitive microchannel plate detector. *Chin. Phys. C* **40**, 096004 (2016). [doi:10.1088/1674-1137/40/9/096004](https://doi.org/10.1088/1674-1137/40/9/096004)

[16] J.H. Tan, J.R. Zhou, Y.S. Song et al., Simulation and optimization of co-doped nMCP used in a neutron imaging detector. *Journal of Harbin Engineering University* **42**, 1792–1799 (2021). [doi:10.11990/jheu.202107067](https://doi.org/10.11990/jheu.202107067)

[17] A.S. Tremsin, J Mcphate, J Vallerga et al., Improved efficiency of high resolution thermal and cold neutron imaging. *Nucl. Instr. Meth. A* **628**, 415 (2011). <https://doi.org/10.1016/j.nima.2010.07.014>

[18] S. Wang, H. Li, C. Cao et al., Optimal calculation of detection efficiency for thermal neutron sensitive microchannel plate. *Acta Phys. Sin.* **64**, 102801 (2015). [doi:10.7498/aps.64.102801](https://doi.org/10.7498/aps.64.102801)

[19] J. Pan, Y. Yang, Y. Tian et al., High detection efficiency neutron sensitive microchannel plate. *JINST* **8**, P01015 (2013). [doi:10.1088/1748-0221/8/01/P01015](https://doi.org/10.1088/1748-0221/8/01/P01015)

[20] J.H. Tan, Y.S. Song, J.R. Zhou et al., Novel method to improve neutron–gamma discrimination for boron-doped nMCPs. *Nucl. Instr. Meth. A* **1047**, 167828 (2023). <https://doi.org/10.1016/j.nima.2022.167828>

[21] A.S. Tremsin, J. B. McPhate, J.V. Vallerga et al., Neutron radiography with sub-15 mm resolution through event centroiding. *Nucl. Instr. Meth. A* **688**, 32–40 (2012). <https://doi.org/10.1016/j.nima.2012.06.005>

[22] A.S. Tremsin, J.V. Vallerga, J.B. McPhate et al., Optimization of high-count rate event counting detector with Microchannel Plates and quad Timepix readout. *Nucl. Instr. Meth. A* **787**, 20–25 (2015). <https://doi.org/10.1016/j.nima.2014.10.047>

[23] G.L. Yang, Z.D. An, W. Jiang et al., Measurement of Br(n,γ) cross sections up to stellar s-process temperatures at the CSNS Back-n. *Nucl. Sci. Tech.* **34**, 180 (2023). <https://doi.org/10.1007/s41365-023-01337-6>

[24] Z.Z. Ren, Y.W. Yang, Y.H. Chen et al., Measurement of the  $^{232}\text{Th}(\text{n},\text{f})$  cross section in the 1–200 MeV range at the CSNS Back-n. *Nucl. Sci. Tech.* **34**, 115 (2023). <https://doi.org/10.1007/s41365-023-01271-7>

[25] X.R. Hu, G.T. Fan, W. Jiang et al., Measurements of the  $^{197}\text{Au}(\text{n}, \gamma)$  cross section up to 100 keV at the CSNS Back-n facility. *Nucl. Sci. Tech.* **32**, 101 (2021). <https://doi.org/10.1007/s41365-021-00931-w>

[26] X.Y. Liu, Y.W. Yang, R. Liu et al., Measurement of the neutron total cross section of carbon at the Back-n white neutron beam of CSNS. *Nucl. Sci. Tech.* **30**, 139 (2019). <https://doi.org/10.1007/s41365-019-0660-9>

[27] Q. Li, G.Y. Luan, J. Bao et al., The 6LiF-silicon detector array developed for real-time neutron monitoring at white neutron beam at CSNS. *Nucl. Instr. Meth. A* **946**, 162497 (2019). <https://doi.org/10.1016/j.nima.2019.162497>

[28] J.Y. Tang, H.T. Jing, H.H. Xia et al., Key nuclear data measurements for advanced fission energy and white neutron source at CSNS. *Atomic Energy Sci. Technol.* **47**, 1089–1095 (2013). doi: [10.7538/yzk.2013.47.07.1089](https://doi.org/10.7538/yzk.2013.47.07.1089)

[29] J.Y. Tang, Q. An, J.B. Bai et al., Back-n white neutron source at CSNS and its applications. *Nucl. Sci. Tech.* **32**, 11 (2021). <https://doi.org/10.48550/arXiv.2101.06567>

[30] D. L. Zhang, P. Cao, Q. Wang et al., System design for precise digitization and readout of the CSNS-WNS BaF2 spectrometer, *Chin. Phys. C* **41**, 159–165 (2017). doi:[10.1088/1674-1137/41/2/026102](https://doi.org/10.1088/1674-1137/41/2/026102)

[31] Q. Wang, P. Cao, X. Qi et al., General-purpose readout electronics for white neutron source at china spallation neutron source. *Rev. Sci. Instrum.* **89**, 013511 (2018). <https://doi.org/10.1063/1.5006346>

[32] Q. Wang, P. Cao, D. Zhang et al., Prototype of field waveform digitizer for BaF2 detector array at CSNS-WNS. *IEEE. T. Nucl. Sci.* **64**, 1988–1993 (2017). doi:[10.1109/TNS.2017.2714707](https://doi.org/10.1109/TNS.2017.2714707)

[33] I. Antcheva, M. Ballintijn, B. Bellenot et al., ROOT — A C++ framework for petabyte data storage, statistical analysis and visualization. *Comput. Phys. Commun.* **180**, 2499–2512 (2009). <https://doi.org/10.48550/arXiv.1508.07749>

[34] D.A. Brown, M.B. Chadwick, R Capote et al., ENDF/B-VIII.0: The 8th Major Release of the Nuclear Reaction Data Library with CIELO-project Cross Sections, New Standards and Thermal Scattering Data. *Nucl. Data Sheets* **148**, 1–142 (2018). <https://doi.org/10.1016/j.nds.2018.02.001>

[35] D.J. Zhao, S Feng, P.J. Chen et al., Conceptual design of a Cs<sub>2</sub>LiLaBr<sub>6</sub> scintillator-based neutron total cross section spectrometer on the back-n beam line at CSNS. *Nucl. Sci. Tech.* **34**, 3 (2023). <https://doi.org/10.1007/s41365-022-01152-5>

[36] Z.W. Ma, J.R. Wang, Z.W. Huang et al., Monte Carlo simulation of 10B doped thermal neutron sensitive microchannel plate. *JINST* **13**, T10002 (2018). doi:[10.1088/1748-0221/13/10/T10002](https://doi.org/10.1088/1748-0221/13/10/T10002)

[37] Y.H. Chen, G.Y. Luan, J. Bao et al., Neutron energy spectrum measurement of the Back-n white neutron source at CSNS. *Eur. Phys. J. A* **55**, 115 (2019). <https://doi.org/10.1140/epja/i2019-12808-1>